UNIVERSITY OF CALIFORNIA,
IRVINE

# Anomalous Friction Behaviors in Graphene-Copper Interface Dictated by Moiré Patterns

THESIS

submitted in partial satisfaction of the requirements
for the degree of

MASTER OF SCIENCE

in Materials Science and Engineering

by

Liming Zhao

Dissertation Committee:
Assistant Professor Penghui Cao, Chair
Associate Professor Tim Rupert
Associate Professor Daniel Mumm

2020

# TABLE OF CONTENTS

# LIST OF FIGURES

# ACKNOWLEDGEMENTS

I would appreciate my committee chair, Assistant Professor Penghui Cao, who provided me with patient and continuous guidance. I have made a great progress on independent research under his scientific training, and I would have not finished this work without his advice. I would also like to express my appreciation to my committee members, Associate Professor Daniel Mumm and Associate Professor Tim Rupert who showed interests in my work and denoted themselves on reviewing my final results.

# ABSTRACT OF THE THESIS

Anomalous Friction Behaviors in Graphene-Copper Interface Dictated by Moiré Patterns

by

Liming Zhao

Master of Science in Materials Science and Engineering

University of California, Irvine, 2020

Assistant Professor Penghui Cao, Chair

This thesis focuses on understanding the role of moiré patterns formed between graphene and metal substrate in governing the interfacial frictional behavior. The frictional system consists of graphene supported on a bulk copper substrate, which is investigated by atomistic simulations. The thesis first discusses moiré patterns appearing between graphene and copper, whose morphology depends on crystallographic orientation and relative positions. Depending on system temperature and the contacting nature, two extreme friction phenomena, namely superlubricity and supersticky, have been found, both of which are mediated by moiré patterns. The superlubricity effect can be achieved by tuning the rotation angle of moiré patterns to high value. However, such a condition only happens in metastable states with high potential energy, which induces the graphene layer spontaneously incline to lower energy state with small rotation angles, causing the disappearance of superlubricity. It is found that introducing grain boundaries in graphene can stabilize the high-angle moiré patterns and therefore retain superlubricity. On the other hand, supersticky effect was found to occur at ultra-low temperatures, at which

stable moiré pattern persists and raises the resistance to sliding. In the end, the thesis provides details on the developed mathematical models, which describe the rotation and translation process of hexagonal moiré patterns, simplifying the generation of moiré patterns due to graphene rotation and lateral sliding movement.

# INTRODUCTION

In recent years, two-dimensional hexagonal materials represented by graphene have become a hot spot in materials science research. A number of studies have carefully examined monolayer graphene from almost all aspects, such as tensile behavior, thermoconductivity, as well as conductivity [1, 2, 3, 4]. Along the way, people have found the generation of moiré patterns in the heterojunctions composed of multiple layers of 2D materials, which bring attractive properties. For example, a sensational discovery verified the superconducting effect in the twisted double-layer graphene, the phenomenon of which can be interpreted as the changing in the energy band by the moiré pattern [5, 6, 7].

Another exciting research trail, also the focus of this thesis, lies in the interfacial frictional behavior [8, 9]. In 2004, Dienwiebel et al. [10] found superlubricity in graphite as well as the role of the rotation angle in controlling friction force. However, they had not unveiled the nature of the rotation angle at the atomistic level. Song et al. [11] explained that the rotation angle actually controls the morphology of moiré patterns, which determines the out-of-plane motion of carbon atoms. A large rotation angle forms smaller moiré patterns and weakens the atomic motion along out-of-plane direction. Therefore, they confirmed that superlubricity only happens in those orientations with high rotation angles.

However, high rotation angle not only brings superlubricity, but also brings instability. The high angle raises the potential energy of graphene, causing a metastable state. It has previously been observed that the graphene spontaneously rotates to a low rotation angle [12], which is not favorable to the appearance of superlubricity. Aimed at

this issue, the thesis first investigated the role of rotation angle in regulating the potential energy. Then, a grain boundary in graphene was introduced to stabilize high-energy moiré patterns that lead to the superlubricity effect.

In addition to superlubricity, it is surprising to find an opponent phenomenon at low temperatures, namely supersticky effect, in the interface of the graphene and the copper substrate. This thesis concludes that the so-called supersticky effect is governed by the moiré pattern strengthening mechanism.

The structure of the thesis is that: (i) Chapter 1 talks about the formation of moiré patterns and gives a basic description of the moiré patterns studied in the following chapters; (ii) Chapter 2 focuses on how potential energy varies with moiré patterns and rotation angles; (iii) Chapter 3 provides the way to stabilize moiré patterns with high potential energy; (iv) Chapter 4 centers on the supersticky effects caused by the moiré pattern strengthening mechanism; (v) Chapter 5 draws the conclusion of the study; (vi) Appendix 1 gives the methods and assembly involved in the study; (vii) Appendix 2 shows the mathematical derivation of the equations to describe the rotation motion and translation motion of moiré patterns, which can explain simulation results.

# CHAPTER 1: Formation of Graphene-Copper Moiré Patterns

The term *moiré* means “watered” in French and was first found in a shimmering silk textile with ripples pattern [13]. Two or more layers of moiré silk with parallel cords are pressed together in a humid ambient. It displays moiré patterns due to misaligned cords that are parallel to each other but have imperfect spacing [14]. Additionally, a moiré pattern is not only generated by two sets of parallel lines, but also by any two patterns of the same type but different periods, such as square and hexagon shown in Figure 1 [15].

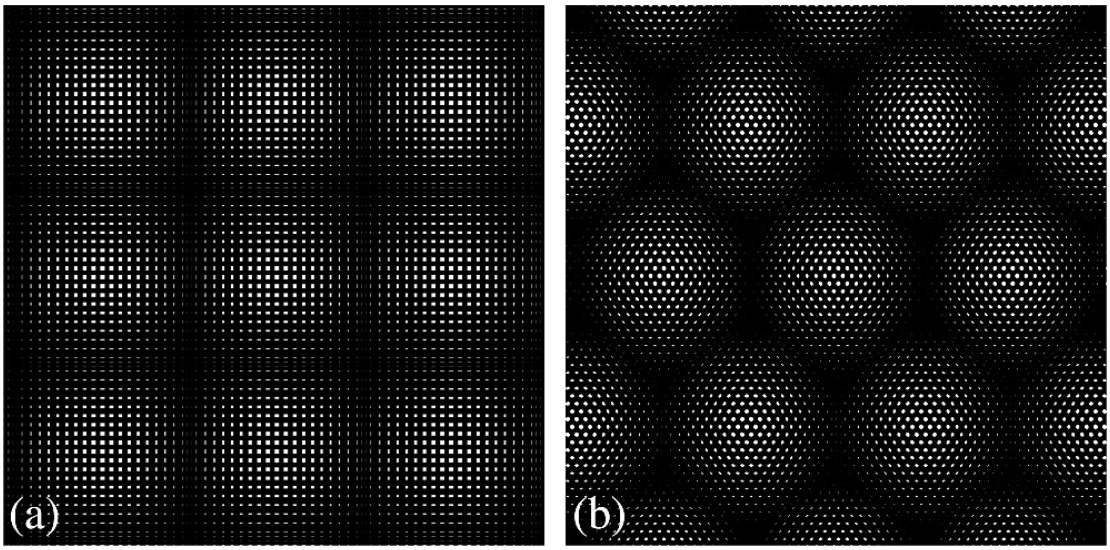


**Figure 1: (a) Square and (b) hexagonal moiré patterns generated by two grids [15].**

The moiré pattern discussed in this thesis emerges from the hexagonal symmetries of the atomic arrangement and comparable lattice constants of copper (111) surface and graphene. One difference between such moiré patterns and those defined by aesthete is that crystallographic moiré patterns not only have periodicity in-plane but also have periodic atomic height fluctuations in the out-of-plane direction. As shown in those circular

yellow regions of Figure 2 (a), carbon atoms accommodate more to the gaps of copper atoms where copper and carbon atoms are misaligned and therefore generate local drops, namely moiré valley. Contrarily, carbon atoms are relatively far away from the copper surface, leading to higher interface spacings in red regions. The atomic arrangement is shown in Figure 2 (b). The amplitude between valleys and peaks is 0.15 angstrom for average. The moiré pattern discussed in the thesis is a typical one generated in the two-dimensional interface. In addition to the Graphene-Copper system, similar patterns have been found in other systems, such as graphene/h-BN [8], which has both hexagonal-symmetric arrangements. Graphene has two degrees of freedom associated with the friction process, i.e., rotation and translation motions, which will be discussed in the following chapters and appendices.

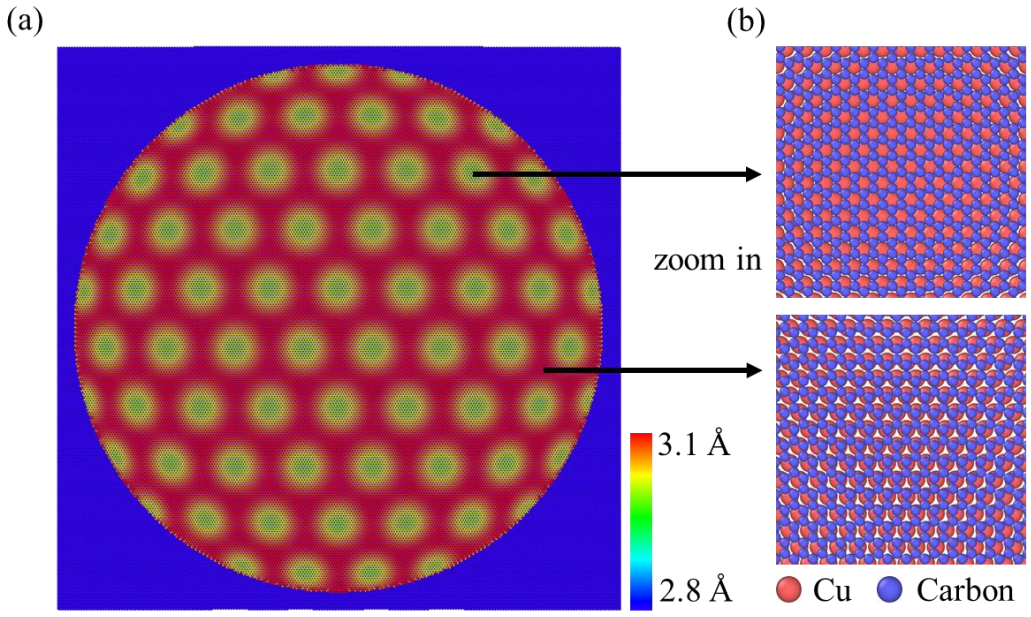


**Figure 2: (a) Atomic height image displaying moiré patterns generating on circular graphene supported on copper (111) surface. (b) Zoom-in images of the moiré valley and peak showing the local atomic arrangement. Graphene and copper atoms are denoted as the blue and red spheres, respectively.**

## CHAPTER 2: Rotation Angle Dependence of Friction and Potential Energy

Studies over the past few years have verified that the friction force tightly depends on the rotation angle between two hexagonal layers [10]. Appendix 2 thoroughly describes the definition and the derivation of the rotation angle. As shown in Figure 3, the frictional force exhibits regularity with a period of 60 ° due to the hexagonal symmetry of the moiré pattern. Only when the rotation angle is relatively large (i.e., higher than 4°), will the so-called superlubricity appear.

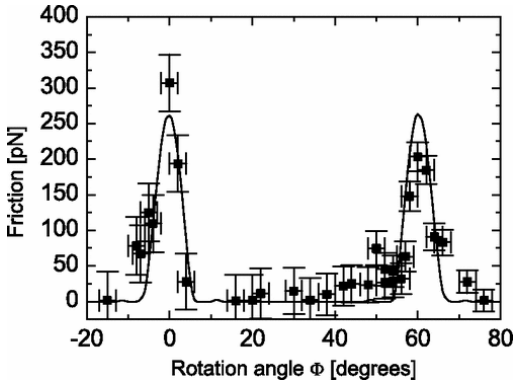


**Figure 3: The variation of the friction force versus the rotation angle [10]**

However, few researchers have been able to draw on any research into the stability of superlubricity. Thereupon, the thesis investigates the stability of the graphene-copper system from the perspective of the potential energy landscape. Figure 4 (a) presents the graphene potential energy as a function of the rotation angle in a period from 0° to 30°. Here, the definition of the angle value is the same as the definition in Figure 3. The energy reaches to the global minimum between 2° and 3°, the degree of which is not favorable to superlubricity. Dynamic simulation results, as provided by Figure 4 (b), prove that a high-

angle state (i.e., 30 degrees) eventually dropped down to the angle of 2.1 degrees, which agrees with the experimental measurement [16]. Therefore, a problem appears: the superlubricity state is restricted by its instability. In the next chapter, the thesis provides a solution to stabilize the superlubricity effect.

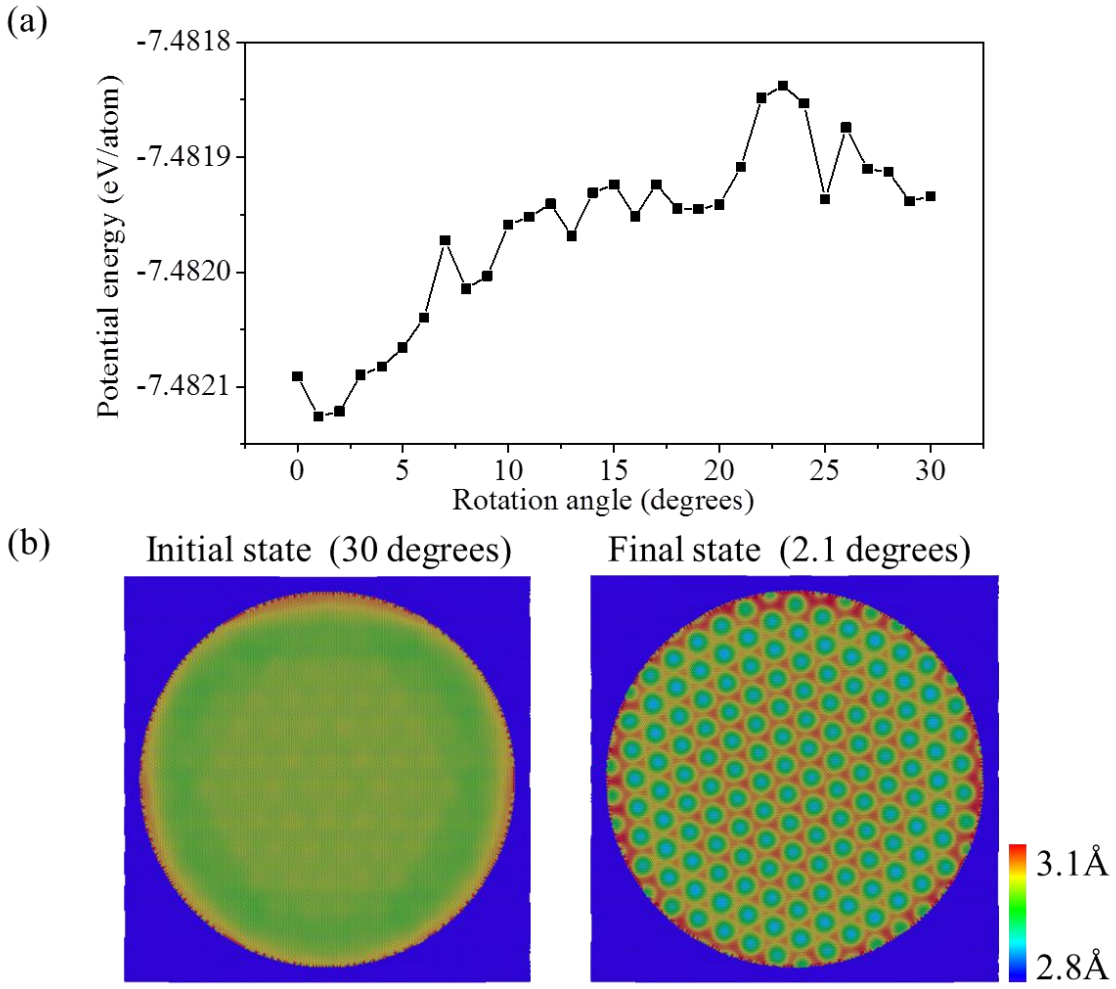


**Figure 4: (a) Graphene potential landscape within a period of the rotation angle from 0° to 30°. (b) The initial state (left) and final state (right) of relaxation. Atoms are colored by their heights.**

## CHAPTER 3: Stabilizing Effect of Grain Boundaries on Moiré patterns

Here, a grain boundary in graphene is developed, generating bi-crystalline graphene, to stabilize high-angle states of graphene. The total twenty of graphene grain boundary structures were systematically presented by previous work [17], including symmetric boundaries (e.g., (2,1)|(2,1), (3,2)|(3,2) and (4,3)|(4,3)) and nonsymmetric boundaries (e.g. (3,1)|(2,2), (5,3)|(4,4) and (6,0)|(4,3)). The indices are defined according to the orientation of the grains along the grain boundary direction [18]. From the perspective of roughness, those grain boundaries are classified as two types: the first type, such as (2,1)|(2,1), (3,2)|(3,2) and (6,0)|(4,3), leads to a more flat graphene layer, while another type, such as (3,1)|(2,2), (5,3)|(4,4) and (4,3)|(4,3), causes a graphene layer to protrude upward at the grain boundary due to high local stress. To get rid of the roughness diturbance, this work selects the first type, e.g., (2,1)|(2,1) as shown in Figure 5 (b), to study the grain boundary effect on moiré patterns.

Dynamic simulation was conducted to verify the stability of the bi-crystalline graphene. Figure 5 (a) shows the pre-relaxing and post-relaxing morphologies of graphene. The period of moiré patterns is 1.2 nm before the relaxation, the value of which is retained after the dynamic relaxation at 1000K for one ns. The same value of the moiré period implies the maintence of the rotation angle. The comparison of the morphologies between Figure 5 (a) and Figure 4 (b) confirms that a grain boundary allows the stable presence of those moiré patterns appearring only in high-angle state. This phenomenon can be explained by the competing mechanism induced by the symmetric grain boundary. Two grains have opposite rotation angles (i.e., $\pm 10.9°$) as well as opposite rotation trends

(clockwise and counterclockwise), which brings great resisance to the rotation of the entire graphene.

In spite of the stability brought from the grain boundary, it is still indispensable to verify the newly-introduced grain boundary has no negative influence on superlubricity. Column III in Figure 6 (c) is corresponding to the friction force of the bi-crystalline graphene, which is much smaller than that of the most stable state of the single-crystalline graphene. Even Column II, the moiré period of which is the same as Column III, has a slightly higher friction force than III. It can be interpreted by the smaller atomic density around the grain boundary. Thus, superlubricity can also happen in bi-crystalline graphene as long as the high-energy moiré patterns in each grain are retained.

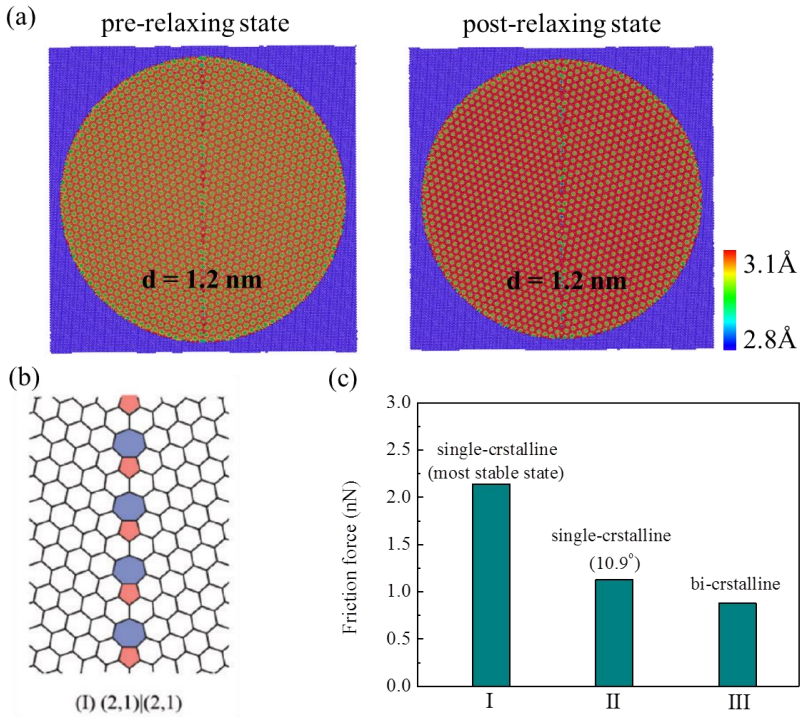


**Figure 5: (a) The pre-relaxing and post-relaxing states of bi-crystal graphene, where atoms are colored by atomic heights. (b) Schematic of (2,1)|(2,1) type grain boundary in graphene [17]. (c) Comparison of friction force in crystalline and bi-crystalline graphene.**

# CHAPTER 4: Supersticky Effect Caused by Moiré Patterns at Ultralow Temperature

Previous chapters introduced the association between moiré patterns and superlubricity. It is somewhat surprising that the moiré pattern in a single-crystalline graphene evokes an opposite effect, namely supersticky, at low temperatures.

Figure 6 exhibits the friction simulation model where the size is consistent with the model in Chapter 2. Graphene is subjected to a normal force evenly distributed on every carbon atoms. The sliding movement of graphene is induced by a spring linked to the center of mass of the graphene layer. The same models are simulated under a broad spectrum of temperatures (e.g., 0.001K, 0.01K, 0.1K, 1K, 10K, and 300K) to unveil the impacts of temperature on the morphologies and interfacial friction force.

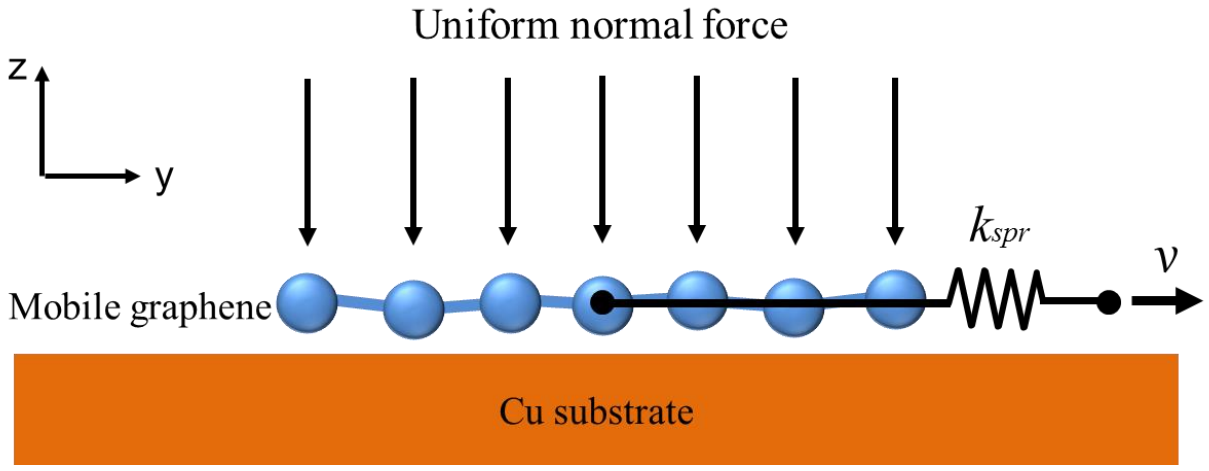


**Figure 6: The schematic of the friction simulation model. A uniform normal force is applied on each carbon atom. The spring has a constant velocity of 0.1 Å/s along the +y direction. Spring constants are defined in x and y directions, and there is no spring force along the z-axis.**

The pre-pulling morphologies of graphene and copper surface are presented in Figure 7 (a) and (b), respectively. To highlight the role of the temperature in governing morphologies, the atomic height mappings at 0.001K and 300K are provided here. Under ultralow temperature, i.e., 0.001K, ordered pit-like moiré patterns appear at the corresponding positions on both the graphene layer and the copper surface, which serve as pinning centers during the sliding process. At 300K, contrarily, having higher energies to escape the constraint of the potential barriers, atoms are more randomly arranged without specific orientations, and therefore the majority of moiré patterns become blurred. Adding normal force preserves and even deepens moiré patterns at 0.001K, while the additional normal force is not beneficial to the reproduction of moiré patterns.

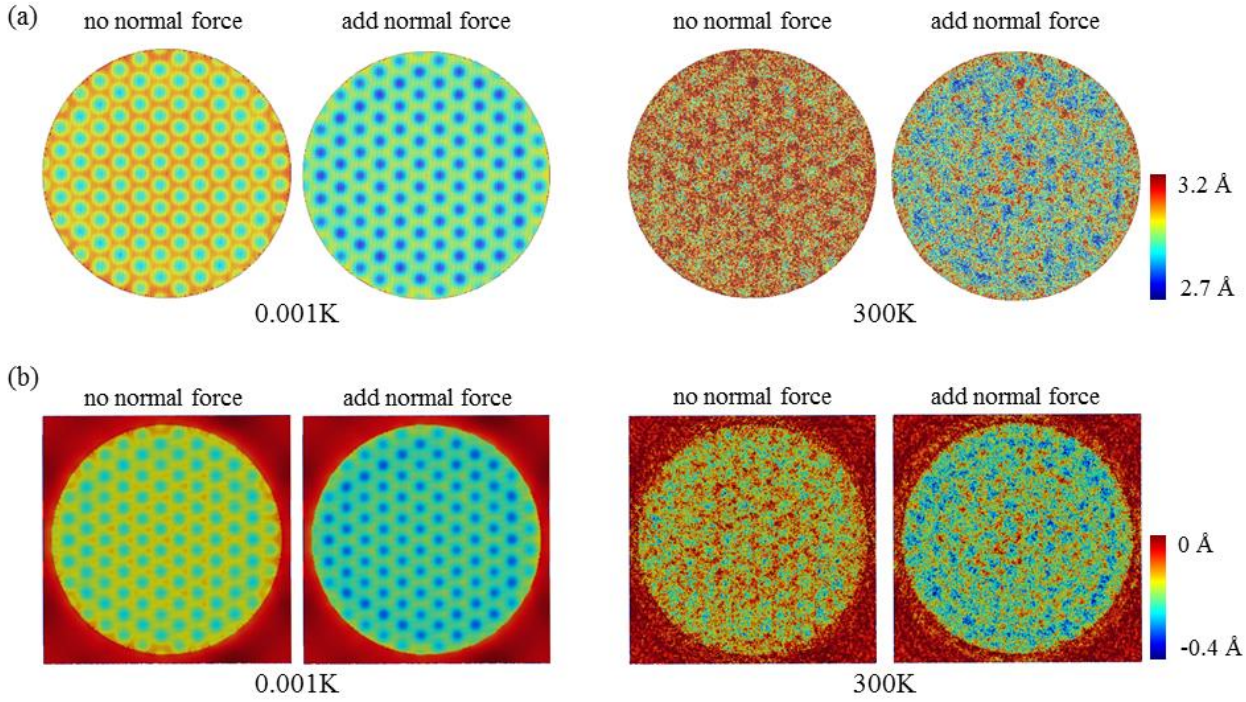


**Figure 7: Pre-pulling morphologies of graphene (a) and copper (111) surface (b) at 0.001K and 300K (as labeled). For both temperatures, morphologies before and after adding normal force are exhibited. Images are colored by atom heights.**

The interficial friction force as a function of the temperature is summarized in Figure 8 (a). It is surprising to observe that the interficial friction at 0.001K is almost a hundred times higher than that at 300K. Friction is much sensitive to temperature below 1K, while such dependence becomes indistinct above 1K. Figure 8 (b) shows force traces during sliding processes, which can be divided into two parts: the velocity of graphene keeps rising but is lower than the spring velocity within the first-nanometer sliding, causing a dramatic increase of the friction. Subsequently, the friction force levels off and the graphene reaches the steady-state sliding motion. A regular pattern of force fluctuation associated with the so-called stick-slip mode can also be seen in Figure 8(b), especially at the lowest temperature, which suggests a dynamic balance of the distance between the graphene and the spring.

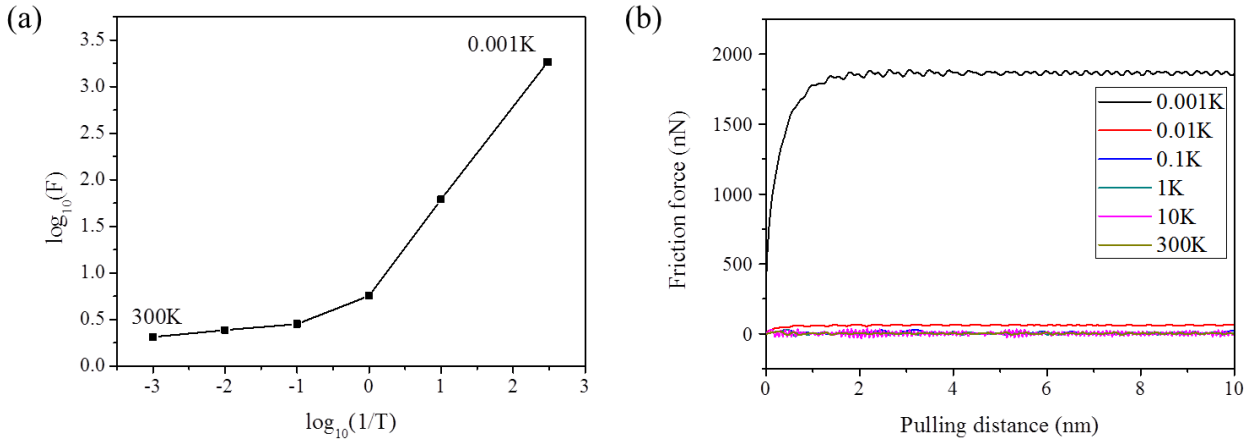


**Figure 8: (a) Variation of interficial friction showing the relationship between temperature and friction force. (b) Force traces at a series of temperatures in a range of six orders of magnitude, i.e., 0.001K, 0.01K, 0.1K, 1K, 10K, and 300K, marked by different colors.**

The change in friction emerges from the change in the morphology. To clearly demonstrate the dependence of morphologies on temperatures during the sliding process, this study respectively selected two stick-slip motions at two typical temperatures, 0.001K and 300K, as shown in Figure 9 (a), and obtained the atomic height mappings at the peak states shown in Figure 9 (b). For the scenario of 0.001K, the comparison of the pre-pulling morphology in Figure 7 (a) and the post-pulling one here attests that moiré patterns are retained during the sliding process. The carbon atoms in the front are raised by around 0.1 Å, which is caused by the uneven unidirectional pulling. On the contrary, atoms are arranged more uniformly at room temperature.

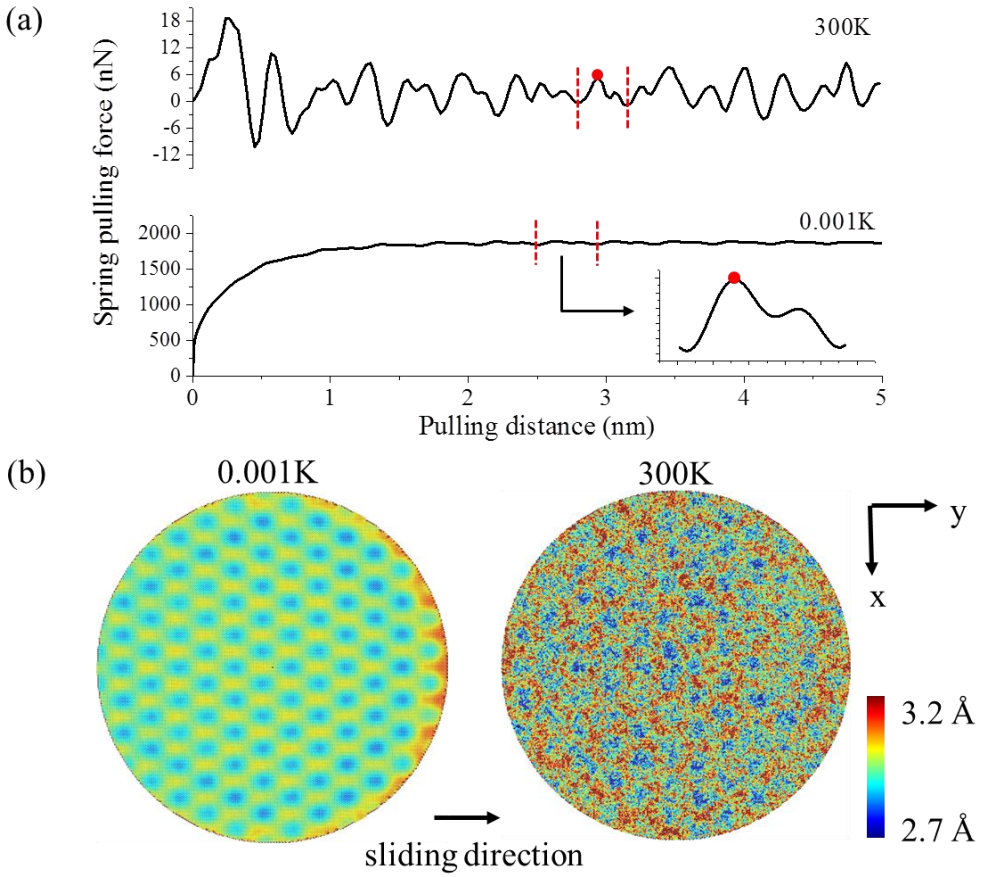


**Figure 9: (a) The selection of peak states from friction traces, denoted by red dots. (b) Graphene morphologies of the chosen states. Atoms are colored by their heights.**

It is notable that the overall atomic height distribution at 0.001K is lower than that at 300K. Thereupon, the growth in friction forces may emerge from the increase in the contacting area. The contacting area is defined as the area occupied by copper atoms within a specific range around graphene atoms. The cutoff range is given a reasonable value larger than the balance distance between copper and carbon atoms in Lennard-Jones potential, e.g., 4 Å. The green and black bars in Figure 10 compare the changes in friction force and contacting area with temperature, respectively. Although lower temperatures indeed result in relatively large contacting areas, contacting areas only expands 1‰ from 300K to 0.001K, which cannot fully explain the supersticky phenomenon.

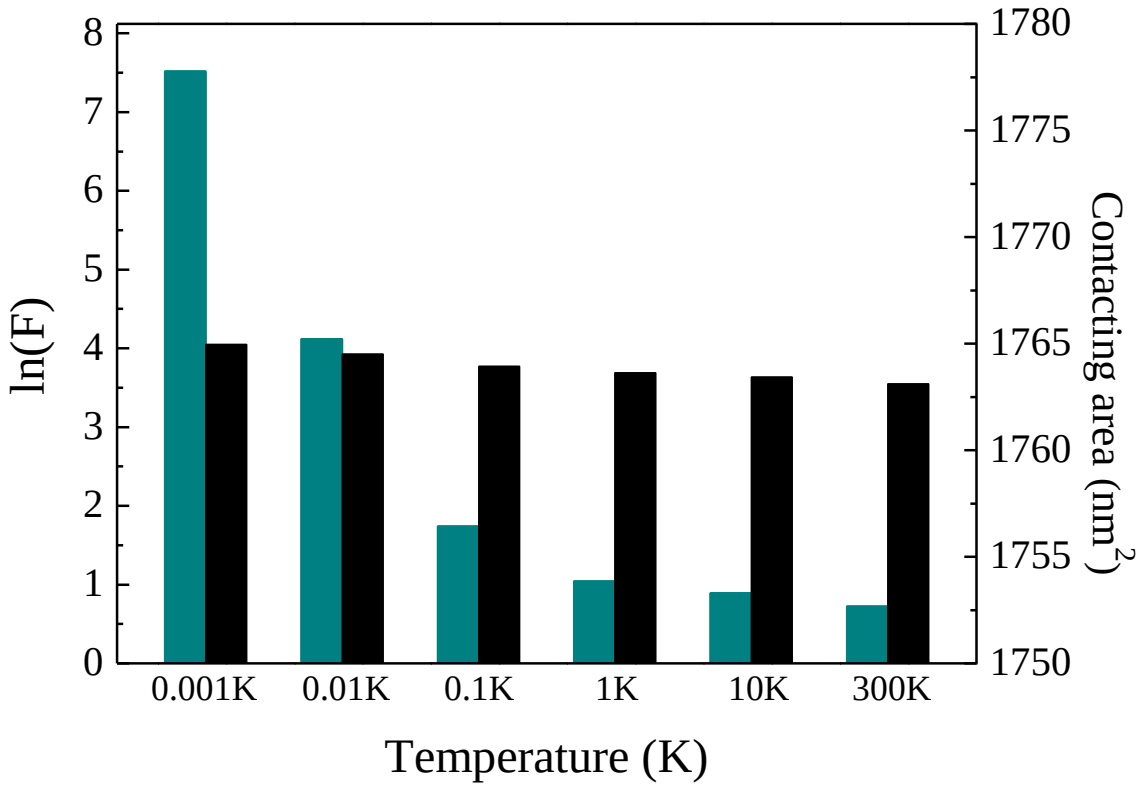


**Figure 10: Temperature dependence of the interficial friction force and the contacting area, colored by dark cyan and black, respectively.**

As the supesticky effect does not completely originate in the change in contacting areas, there must be a decisive factor governing in the supersticky phenomenon. The atomic force between graphene and copper atoms was then examined to clarify the origin of the supersticky effect at low temperatures. The atomic force mappings in Figure 11(a) only include copper atoms on the top layer that applied friction force on graphene atoms. The copper atoms underneath the top layer are reasonably excluded since their friction forces are smaller two orders of magnitude than that exerted by atoms on the top layer. The atomic force mappings exhibit the same periodicity and regularity as the moiré patterns in Figure 9 (b), which is particularly distinct at 0.001K. The patterns are relatively faint or even disappeared in some regions at 300K, such as in the top left and right area, which implies little atomic force, no matter pulling or dragging force, exerted by copper atoms on graphene. On the contrary, the atomic force mapping manifests a series of dark blue areas separated by lighter banded red areas at 0.001K, which are corresponding to the orange columns of -0.045nN∼-0.075nN and 0.03nN ∼0.045nN in Figure 11 (b), respectively. Those blue regions applying dragging force on the graphene serve as pinning centers, which should be the significant contributor to the supersticky effect. In addition, the edge effect on the atomic friction force becomes more explicit at 0.001K: some copper atoms in the front and back exert extreme large atomic friction forces, the phenomenon of which is hard to be observed at 300K. The force distributions in Figure 11 (b) quantify such edge effect. Although the edge effect produces both dragging force and pulling force, the dragging force is more dominant in the marginal area, and thereby leading to the supersticky effect.

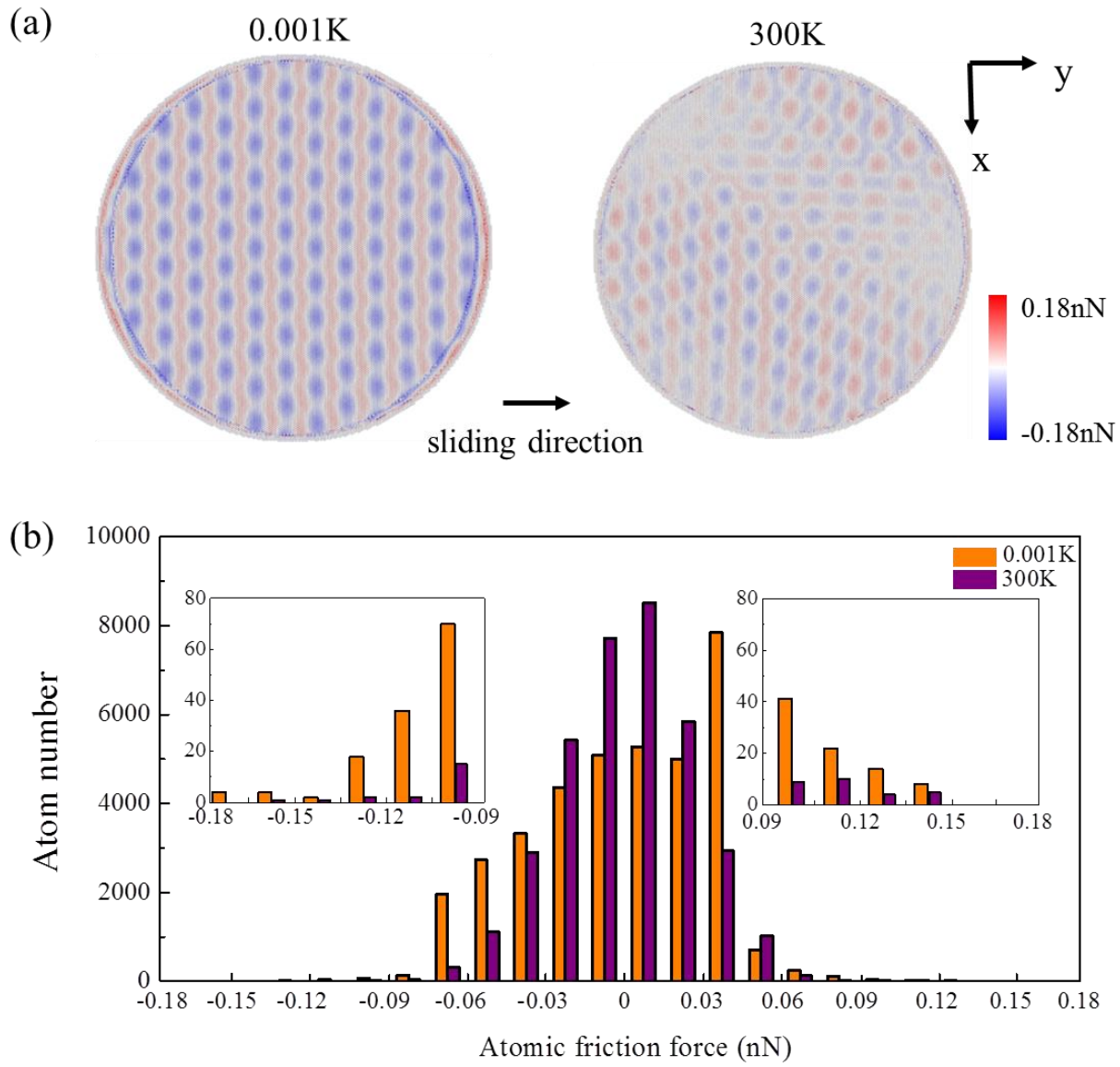


**Figure 11: (a) Copper surface mappings colored by the atomic force applied on the graphene. Only copper atoms on the top layer that contributed to the friction force were included. The positive force represented the force pulling graphene to move forward (+y direction), and negative force stands for the force dragging graphene to move backward (-y direction). (b) The corresponding distribution of the atomic force plotted in (a).**

Following the atomic force mappings, the morphologies of graphene and copper were deliberately checked to specify the source of pinning centers. The right column in Figure 12 (a) showed the enlarged views of the morphologies and atomic force mapping at the same site. Considering that graphene is pulled to the right, one can observe that the morphology fluctuation of graphene and copper is not as consistent as the pre-pulling state. Instead, the valley of moiré patterns on graphene slightly deviates to the right compared with the counterpart on the copper surface. The evolution hysteresis of moiré patterns on the copper surface is caused by the pinning effect of the underlying copper atoms to the surface atoms. In the mapping of the atomic force, the pinning center appears between the moiré valleys on the graphene and the copper. As illustrated by the schematic in Figure 12 (b), when the valley on graphene slides across the peak on copper, the pinning center emerges in the region where graphene and copper are locally squeezed. Moreover, copper atoms move weakly out-of-plane due to the low temperature, which raises the difficulty for copper atoms to accommodate the change in graphene. Therefore, the so-called moiré pattern strengthening mechanism plays a vital role in the supersticky phenomenon. On the contrary, such a strengthening mechanism is insufficient at room temperature. As shown in Figure 13 (a), due to the relatively high energy of atomic thermal vibration at room temperature, moiré patterns on both the graphene layer and copper surface are destroyed or blurred. Further, Figure 13 (b) provides more precise information. The atomic height distribution at 300K exhibits a style of Gaussian distribution governed by the thermal vibration, rather than moiré patterns. In contrast, both graphene atoms and copper atoms have preferred heights for forming moiré patterns at ultralow temperature.

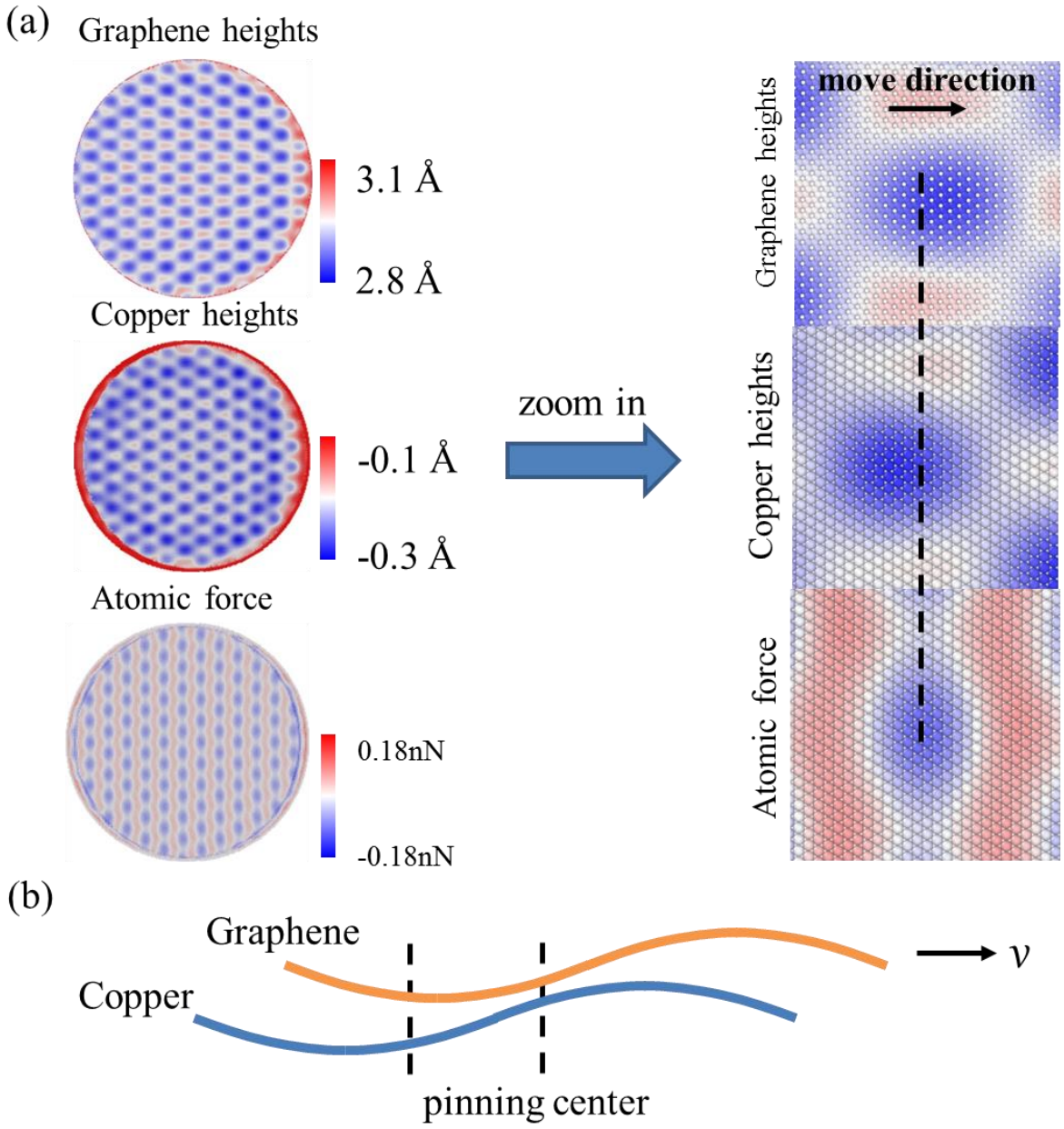


**Figure 12: (a) The global and enlarged views of the atomic force and height mappings. Enlarged views display the same site. (b) Schematic of the graphene and copper morphologies.**

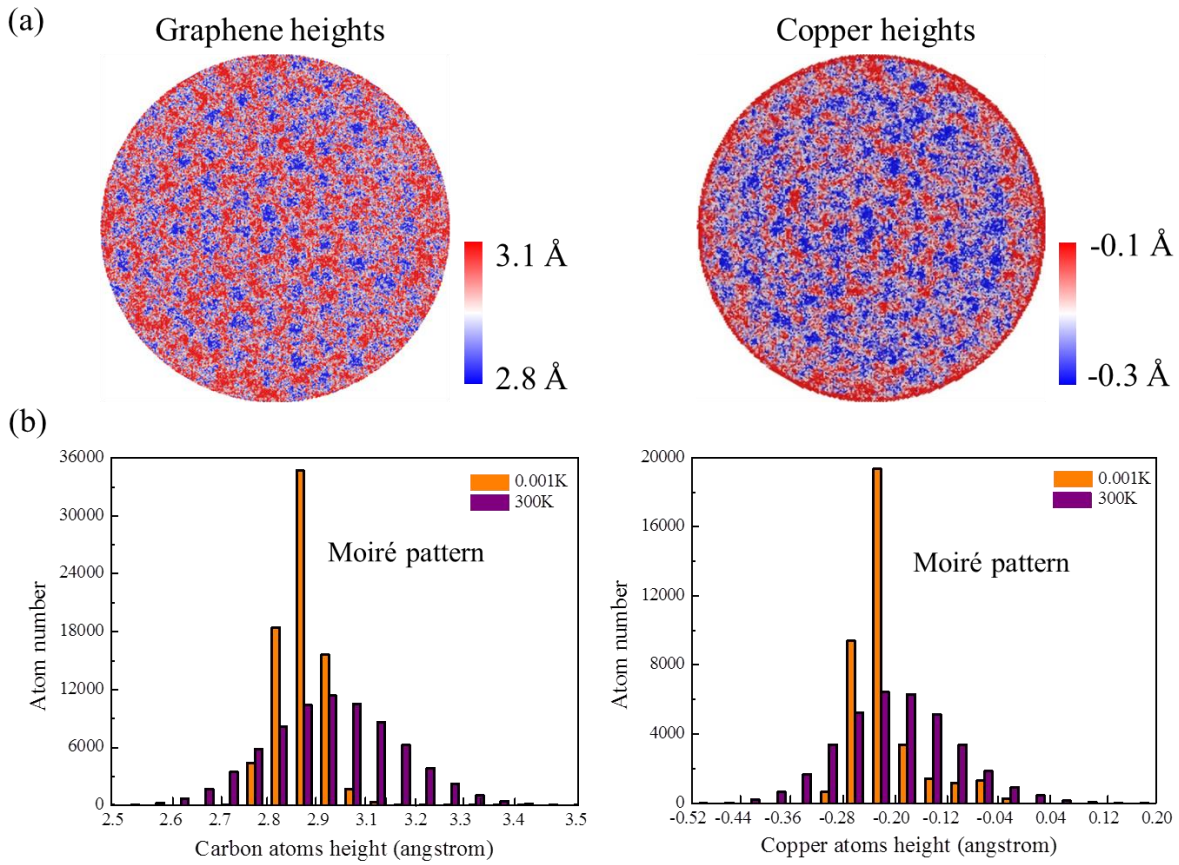


**Figure 13: (a) Morphologies of graphene and copper at the post-pulling state under 300K. (b) Histograms of atomic height distribution for graphene and copper.**

After the discovery of the moiré pattern strengthening mechanism, the association between stick-slip mode and moiré patterns is elaborated by examining five critical states within one stick-slip mode, as marked in Figure 14 (a). The morphologies of these states are sequentially shown in Figure 14 (b). It is worth noting that graphene atoms only move forward by approximately 0.4 nm during a stick-slip period, which is equal to the copper lattice constant along y-direction, i.e. $[11\bar{2}]$ direction, while the moiré pattern on graphene moves by 8.1 nm. The phenomenon can be well described by Equation (13) in Appendix 2, $||t_m|| = \frac{d_m}{a_g}A$, in which $||t_m||$ and $A$ are the displacement of moiré patterns and graphene

atoms, respectively. The term $\frac{d_m}{a_g}$ serves as the amplification factor. The symbol $d_m$ and $a_g$ stand for the period of moiré patterns and graphene lattice constant, so one can draw that the displacement of the moiré pattern is 20 times greater than that of graphene atoms. Appendix 2 develops the systematic derivation of this equation.

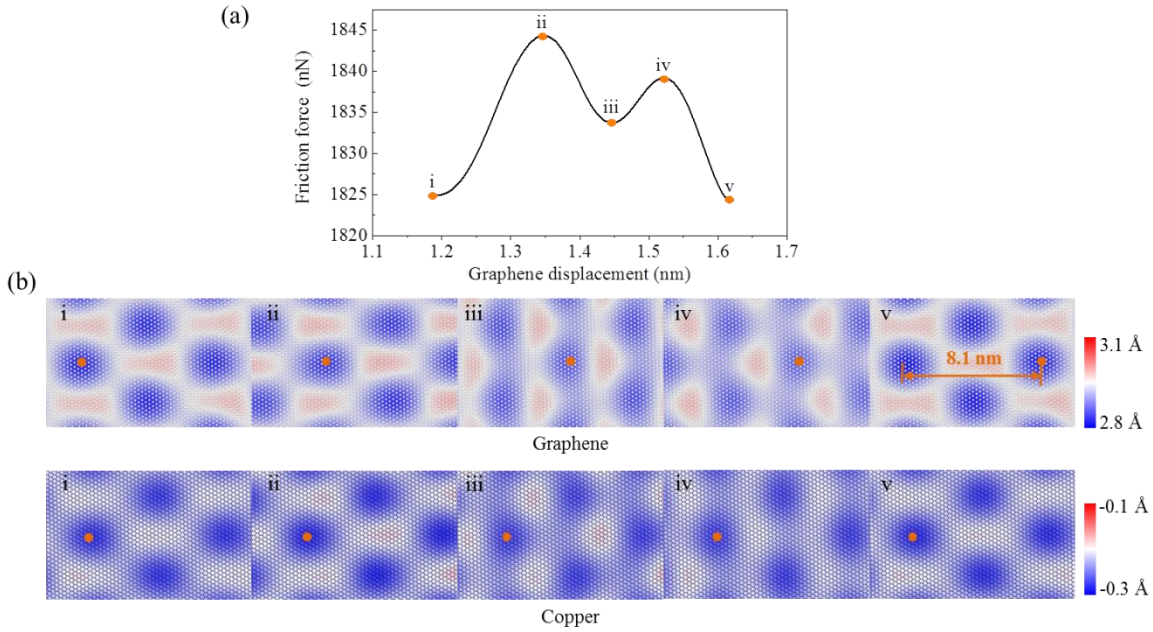


**Figure 14: (a) Friction force trace showing a single stick-slip mode. (b) Morphologies of graphene and copper at the valley or peak states marked in (a). All images showed the same site. The orange dot tracked the same moiré valley.**

# CHAPTER 5: Summary and Conclusions

The focus of this thesis lies in the moiré governing superlubricity and supersticky, appearing in the heterojunction of graphene and copper (111) surface. While a variety of studies have suggested that superlubricity can be achieved only at high-angle states, this thesis explores the stability of superlubricity, which has received scant attention. The atomistic simulation attests to the instability of the states where superlubricity appears. Graphene prefers to rotate to a small-angle state of lower potential energy, causing the disappearance of superlubricity. It is found that grain boundaries can be employed to stabilize the superlubricity state by introducing the competing effect between two grains. Secondly, the supersticky effect is observed at ultralow temperatures, which stems from the generation of pinning centers prompted by the moiré pattern strengthening mechanism. This strengthening effect becomes weakened as increasing temperature, and disappears at room temperature due to the destruction of moiré patterns by atomic thermal vibration. The physical insights gained from this study can be of assistance to control the interfacial interactions and friction behavior, therefore regulate the growth and exfoliation of 2D materials.

# REFERENCES


1. Mortazavi, B. and Ahzi, S., 2013. Thermal conductivity and tensile response of defective graphene: A molecular dynamics study. Carbon, 63, pp.460-470.
2. Jhon, Y.I., Jhon, Y.M., Yeom, G.Y. and Jhon, M.S., 2014. Orientation dependence of the fracture behavior of graphene. Carbon, 66, pp.619-628.
3. Falkovsky, L.A. and Varlamov, A.A., 2007. Space-time dispersion of graphene conductivity. The European Physical Journal B, 56(4), pp.281-284.
4. Balandin, A.A., Ghosh, S., Bao, W., Calizo, I., Teweldebrhan, D., Miao, F. and Lau, C.N., 2008. Superior thermal conductivity of single-layer graphene. Nano letters, 8(3), pp.902-907.
5. Cao, Y., Fatemi, V., Fang, S., Watanabe, K., Taniguchi, T., Kaxiras, E. and Jarillo-Herrero, P., 2018. Unconventional superconductivity in magic-angle graphene superlattices. Nature, 556(7699), pp.43-50.
6. Cao, Y., Rodan-Legrain, D., Rubies-Bigorda, O., Park, J.M., Watanabe, K., Taniguchi, T. and Jarillo-Herrero, P., 2020. Tunable correlated states and spin-polarized phases in twisted bilayer–bilayer graphene. Nature, pp.1-6.
7. Cao, Y., Rodan-Legrain, D., Park, J.M., Yuan, F.N., Watanabe, K., Taniguchi, T., Fernandes, R.M., Fu, L. and Jarillo-Herrero, P., 2020. Nematicity and Competing Orders in Superconducting Magic-Angle Graphene. arXiv preprint arXiv:2004.04148.
8. Leven, I., Krepel, D., Shemesh, O. and Hod, O., 2013. Robust superlubricity in graphene/h-BN heterojunctions. The journal of physical chemistry letters, 4(1), pp.115-120.
9. Liu, S.W., Wang, H.P., Xu, Q., Ma, T.B., Yu, G., Zhang, C., Geng, D., Yu, Z., Zhang, S., Wang, W. and Hu, Y.Z., 2017. Robust microscale superlubricity under high contact pressure enabled by graphene-coated microsphere. Nature communications, 8(1), pp.1-8.
10. Dienwiebel, M., Verhoeven, G.S., Pradeep, N., Frenken, J.W., Heimberg, J.A. and Zandbergen, H.W., 2004. Superlubricity of graphite. Physical review letters, 92(12), p.126101.

11. Song, Y., Mandelli, D., Hod, O., Urbakh, M., Ma, M. and Zheng, Q., 2018. Robust microscale superlubricity in graphite/hexagonal boron nitride layered heterojunctions. Nature materials, 17(10), pp.894-899.
12. He, R., Zhao, L., Petrone, N., Kim, K.S., Roth, M., Hone, J., Kim, P., Pasupathy, A. and Pinczuk, A., 2012. Large physisorption strain in chemical vapor deposition of graphene on copper substrates. Nano letters, 12(5), pp.2408-2413.
13. Hills, P., 1999. Venetian colour: marble, mosaic, painting and glass, 1250-1550. Yale University Press.
14. Oster, G. and Nishijima, Y., 1963. Moiré patterns. Scientific American, 208(5), pp.54-63.
15. Saveljev, V., Kim, S.K. and Kim, J., 2018. Moiré effect in displays: a tutorial. Optical Engineering, 57(3), p.030803.
16. He, R., Zhao, L., Petrone, N., Kim, K.S., Roth, M., Hone, J., Kim, P., Pasupathy, A. and Pinczuk, A., 2012. Large physisorption strain in chemical vapor deposition of graphene on copper substrates. Nano letters, 12(5), pp.2408-2413.
17. Zhang, J., Zhao, J. and Lu, J., 2012. Intrinsic strength and failure behaviors of graphene grain boundaries. ACS nano, 6(3), pp.2704-2711.
18. Wei, Y., Wu, J., Yin, H., Shi, X., Yang, R. and Dresselhaus, M., 2012. The nature of strength enhancement and weakening by pentagon–heptagon defects in graphene. Nature materials, 11(9), pp.759-763.
19. Zeller, P. and Günther, S., 2014. What are the possible moiré patterns of graphene on hexagonally packed surfaces? Universal solution for hexagonal coincidence lattices, derived by a geometric construction. New Journal of Physics, 16(8), p.083028.
20. Coraux, J., Plasa, T.N., Busse, C. and Michely, T., 2008. Structure of epitaxial graphene on Ir (111). New Journal of Physics, 10(4), p.043033.

# Appendix 1: Methods and Assembly

**Methods:** Lammps is employed to establish models and conduct molecular dynamics simulations. The simulations are carried out under the constant-volume and constant-temperature (NVT) ensembles. The interactions between copper atoms are described by the Embedded Atom Model (EAM), and those within the graphene described by the Adaptive Intermolecular Reactive Empirical Bond Order (AIREBO). The interfacial force between copper and carbon is described by Lennard-Jones potential. Dynamics simulation results are visualized by Ovito.

**Graphene Assembly:** A circular single-crystalline graphene with a radius of 25 nm is generated perpendicular to the z-axis. The lattice constant of graphene is 2.46 angstrom. The bi-crystalline graphene is developed by cutting and splicing two single-crystalline graphene sheets. To create (2,1)|(2,1) type of grain boundary, two single-crystalline graphene with -10.9° and 10.9° rotation angles are first generated, and cut each of them into two identical parts. Then, splice the left and right halves of the two graphene sheets together. Carefully check the arrangement of atoms along the grain boudary and manually add or delete carbon atoms so that it forms a complete bi-crystalline graphene after the minimization. The radius of bi-crystalline graphene is maintained to 25 nm.

**Copper Assembly:** The bulk copper substrate is generated with a size of 53 nm, 53 nm, and 3 nm in x, y, and z-axis, respectively. The lattice constant is 3.615 angstrom. Copper is oriented as $[1\bar{1}0]$ in the x-axis, $[11\bar{2}]$ in y-axis and [111] in the z-axis. For the sake of the stability of the whole system, the bottom third of Cu atoms were frozen during the dynamics simulation.

# Appendix 2: Derivation of Moiré Pattern Rotation and Translation Motion

**Rotation motion:**

The relationship between the rotation angle and moiré patterns periodicity has been examined by previous works [19]. Here, a continuous theory used to describe this relationship is summarized. First, as shown in Figure 15 (a), the initial orientation (0 degrees) is defined as: the armchair direction of the graphene is parallel along <110> of the copper substrate, and the zigzag direction is parallel along <112> of the copper surface. Using 60° angle notation, $\mathbf{a_{g1}}$, $\mathbf{a_{g2}}$, and $\mathbf{a_{c1}}$, $\mathbf{a_{c2}}$ are defined as two sets of primitive translation vectors of the graphene and copper, respectively. The vectors $\mathbf{a_{g1}}$ and $\mathbf{a_{g2}}$ are symmetric about the x-axis, orienting at an angle of 30° to it, and $\mathbf{a_{c1}}$ points to the positive direction of the x-axis. The origin of the Cartesian coordinate system does not necessarily need to coincide with a carbon atom, because all initial states can be found in a system due to the lattices mismatch, which means that any other origin points are equivalent to the above-defined state. Through Fourier transform, the reciprocal vectors of graphene and Cu revealed in Figure15 (b) are marked as $\mathbf{b_{gi}}$ and $\mathbf{b_{ci}}$, respectively. The vectors of moiré pattern $\mathbf{k_{m1}}$ and $\mathbf{k_{m2}}$ are expressed as the function of $\mathbf{b_{gi}}$ and $\mathbf{b_{ci}}$:

$$\boldsymbol{k}_{m1} = \boldsymbol{b}_{g1} - \boldsymbol{b}_{c2}, \boldsymbol{k}_{m2} = \boldsymbol{b}_{g2} - \boldsymbol{b}_{c1}. \tag{1}$$

Suppose that the graphene layer rotates θ degree counterclockwise around the origin. The primitive translation vectors are described as:

$$\begin{cases} \boldsymbol{a}_{g1} = a_g \cos(\frac{\pi}{6} + \theta)\hat{\boldsymbol{x}} + a_g \sin(\frac{\pi}{6} + \theta)\hat{\boldsymbol{y}}, \\ \boldsymbol{a}_{g2} = a_g \cos(-\frac{\pi}{6} + \theta)\hat{\boldsymbol{x}} + a_g \sin(-\frac{\pi}{6} + \theta)\hat{\boldsymbol{y}}, \\ \boldsymbol{a}_{c1} = a_c\hat{\boldsymbol{x}}, \\ \boldsymbol{a}_{c2} = \frac{1}{2}a_c\hat{\boldsymbol{x}} + \frac{\sqrt{3}}{2}a_c\hat{\boldsymbol{y}}, \end{cases} \tag{2}$$

where $a_g$ and $a_c$ are lattice constants for graphene and the (111) plane of Cu, respectively.

Based on Equation (2), the reciprocal vectors are solved as:

$$\begin{cases} \boldsymbol{b_{g1}} = \frac{4\pi}{\sqrt{3}a_g}\left(\sin(-\frac{\pi}{6}+\theta)\hat{\boldsymbol{x}} - \cos(-\frac{\pi}{6}+\theta)\hat{\boldsymbol{y}}\right), \\ \boldsymbol{b_{g2}} = \frac{4\pi}{\sqrt{3}a_g}\left(-\sin(\frac{\pi}{6}+\theta)\hat{\boldsymbol{x}} + \cos(\frac{\pi}{6}+\theta)\hat{\boldsymbol{y}}\right), \\ \boldsymbol{b_{c1}} = \frac{2\pi}{a_c}\left(\hat{\boldsymbol{x}} - \frac{1}{\sqrt{3}}\hat{\boldsymbol{y}}\right), \\ \boldsymbol{b_{c2}} = \frac{4\pi}{\sqrt{3}a_c}\hat{\boldsymbol{y}}. \end{cases} \tag{3}$$

Therefore, the moiré vectors are obtained by combining Equation (1) and (3):

$$\begin{cases} \boldsymbol{k_{m1}} = \frac{4\pi}{\sqrt{3}a_g}\sin(-\frac{\pi}{6}+\theta)\hat{\boldsymbol{x}} - \left(\frac{4\pi}{\sqrt{3}a_g}\cos(-\frac{\pi}{6}+\theta) + \frac{4\pi}{\sqrt{3}a_c}\right)\hat{\boldsymbol{y}}, \\ \boldsymbol{k_{m2}} = -\left(\frac{4\pi}{\sqrt{3}a_g}\sin(\frac{\pi}{6}+\theta) + \frac{2\pi}{a_c}\right)\hat{\boldsymbol{x}} + \left(\frac{4\pi}{\sqrt{3}a_g}\cos(\frac{\pi}{6}+\theta) + \frac{2\pi}{\sqrt{3}a_c}\right)\hat{\boldsymbol{y}}. \end{cases} \tag{4}$$

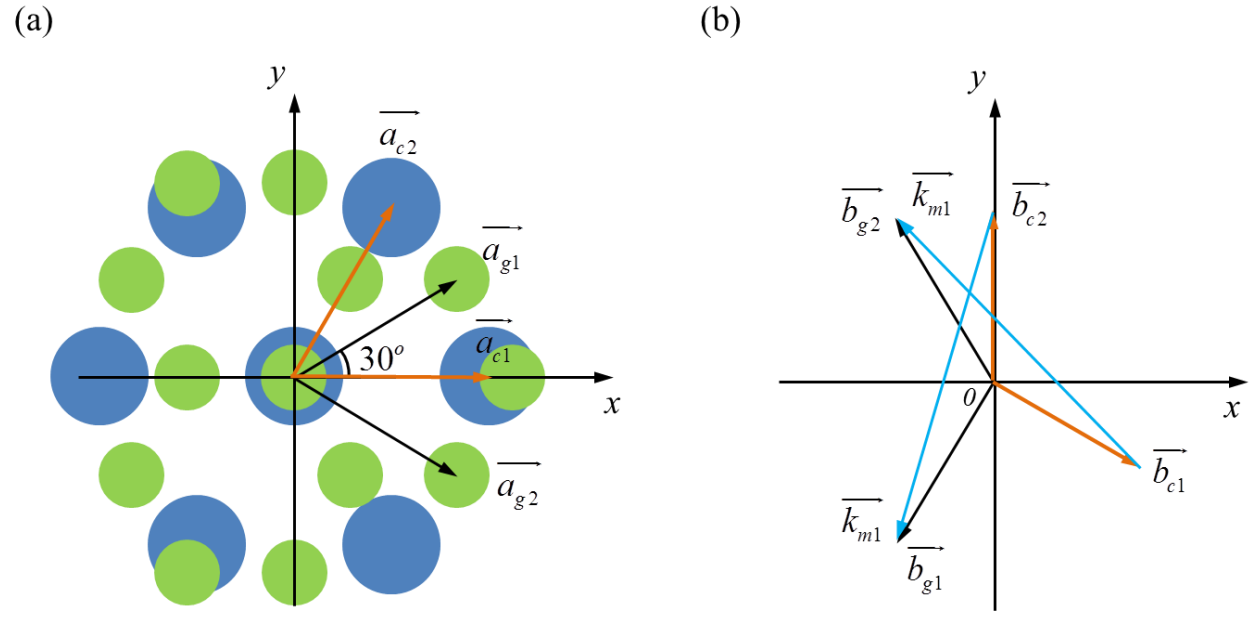


**Figure 15: (a) Schematic showing the initial orientation of graphene and copper substrate. Green and blue circles respectively represent graphene and copper atoms. (b) The basis vectors of graphene, copper, and moiré patterns in reciprocal space, denoted by black, orange, and blue vectors, respectively.**

Since$|\mathbf{k_{m1}}|=|\mathbf{k_{m2}}|$, we only consider $\mathbf{k_{m1}}$ in the following step. The spacing of the (100) plane of a moiré lattice equals $\frac{2\pi}{|\mathbf{km1}|}$. Thus, the expression of a hexagonal moiré pattern periodicity $d_m$ is written as:

$$d_m = \frac{2\pi}{\frac{\sqrt{3}}{2}|\boldsymbol{k}_{m1}|} = \frac{1}{\sqrt{\frac{1}{a_g^2} + \frac{1}{a_c^2} - \frac{2}{a_g a_c}\cos(-\frac{\pi}{6} + \theta)}}. \quad (5)$$

Then, it is worth noting that the shortest moiré lattice vector in the reciprocal space is associated with the moiré period, and other relatively long vectors only affect the contrast of real space images [19]. Therefore, we can modify the phase angle in Equation (5) to obtain the final expression of $d_m$ as follows:

$$d_m = \frac{1}{\sqrt{\frac{1}{a_g^2} + \frac{1}{a_c^2} - \frac{2}{a_g a_c}\cos(\theta)}}. \quad (6)$$

The continuous curve in the valid area is presented in Figure 16. The periodicity for any other rotation angles can be inferred from this curve due to the six-fold symmetry.

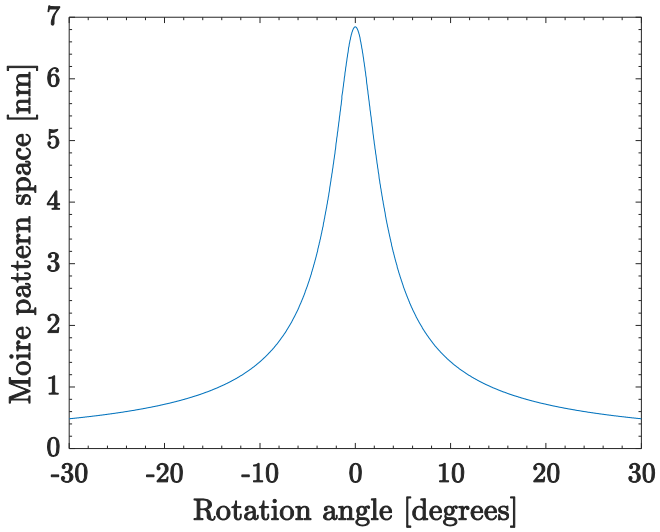


**Figure 16: Relation between moiré spacing and rotation angle of the Graphene-Copper system.**

**Translation motion:**

The friction process of the graphene-copper system can be abstracted into the translational movement of the moiré pattern. The research to date has focused on the rotation motion rather than translation motion. Therefore, this thesis presents an approach to address the issue by the continuous theorem.

As shown in Figure 17, the gliding vector of graphene **t** has two orthogonal unit components $\mathbf{t_{g1}}$ and $\mathbf{t_{g2}}$. The length of the glide vector **t** of the graphene layer is assumed to be *A*, and the angle with respect to the x-axis is denoted by α. Therefore, glide vector **t** is written as:

$$\boldsymbol{t} = A \begin{bmatrix} \cos(\alpha-\theta) & \sin(\alpha-\theta) \end{bmatrix} \begin{bmatrix} \boldsymbol{t_{g1}} \\ \boldsymbol{t_{g2}} \end{bmatrix}. \tag{7}$$

Similarly, the gilding motion of moiré pattern $\mathbf{t_m}$ is expressed by two unit basic vectors $\mathbf{t_{m1}}$ and $\mathbf{t_{m2}}$. Every time, the graphene layer moves by a period $a_g$ along $\mathbf{t_{g1}}$ direction, the moiré pattern moves by a period $d_m$ along $\mathbf{t_{m1}}$ direction. The situation is the same for another set of two basic vectors, $\mathbf{t_{g2}}$ and $\mathbf{t_{m2}}$. Therefore, tm is expressed as:

$$\boldsymbol{t_m} = A\frac{d_m}{a_g} \begin{bmatrix} \cos(\alpha-\theta) & \sin(\alpha-\theta) \end{bmatrix} \begin{bmatrix} \boldsymbol{t_{m1}} \\ \boldsymbol{t_{m2}} \end{bmatrix}. \tag{8}$$

To better present how graphene and moiré pattern move, translation vectors **t** and $\mathbf{t_m}$ are decomposed along x-axis and y-axis:

$$\boldsymbol{t} = A \begin{bmatrix} \cos(\alpha) & \sin(\alpha) \end{bmatrix} \begin{bmatrix} \hat{\boldsymbol{x}} \\ \hat{\boldsymbol{y}} \end{bmatrix}, \tag{9}$$

$$\boldsymbol{t_m} = A\frac{d_m}{a_g} \begin{bmatrix} \cos(\alpha-\theta) & \sin(\alpha-\theta) \end{bmatrix} \begin{bmatrix} \cos(\varphi) & \sin(\varphi) \\ -\sin(\varphi) & \cos(\varphi) \end{bmatrix} \begin{bmatrix} \hat{\boldsymbol{x}} \\ \hat{\boldsymbol{y}} \end{bmatrix}, \tag{10}$$

where φ is the rotation angle of the moiré pattern, which is a function of the rotation angle of graphene θ and the lattice constants [19]:

$$\varphi = \arccos\left(\frac{a_c\cos(\theta) - a_g}{\sqrt{a_g^2 + a_c^2 - 2a_c a_g\cos(\theta)}}\right). \tag{11}$$

Equation (10) is further rewritten as a simpler form as follows:

$$\boldsymbol{t_m} = A\frac{d_m}{a_g}\begin{bmatrix}\cos(\alpha-\theta+\varphi) & \sin(\alpha-\theta+\varphi)\end{bmatrix}\begin{bmatrix}\hat{\boldsymbol{x}}\\ \hat{\boldsymbol{y}}\end{bmatrix}. \tag{12}$$

Therefore, the translation distance of moiré pattern $||\mathbf{t_m}||$ is obtained as:

$$\|\boldsymbol{t_m}\| = \sqrt{\left(A\frac{d_m}{a_g}\cos(\alpha-\theta+\varphi)\right)^2 + \left(A\frac{d_m}{a_g}\sin(\alpha-\theta+\varphi)\right)^2} = A\frac{d_m}{a_g}. \tag{13}$$

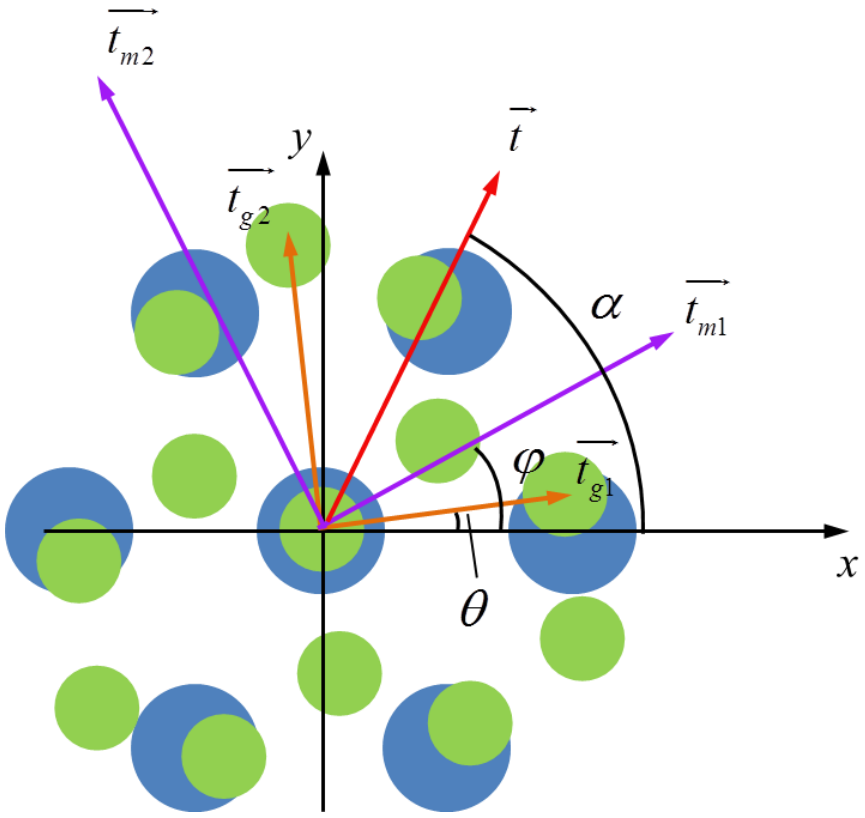


**Figure 17: Schematic of the translation model where graphene and copper atoms are denoted as green and blue circles, respectively.**

Equation (13) indicates that the translation distance of the moiré pattern is a linear function of the gliding distance of the graphene layer for all configurations, and the scale factor between them is $\frac{d_m}{a_g}$. Because the lattice constant of $a_g$ is a constant, the slope is solely determined by the periodicity of the moiré pattern.

To further specify the link between graphene and moiré pattern translation, the translation angle of a moiré pattern, γ, is expected to be expressed as a function of the translation angle of graphene α. This can be derived from Equation (12):

$$\gamma = \alpha - \theta + \varphi, \qquad \alpha \in [-30°, 30°]. \tag{14}$$

Graphene, copper substrate, and moiré pattern all have hexagonal symmetry, the range of α can be reduced to [-30°, 30°]. Considering a particular case when the graphene rotation angle θ is equal to 0, φ equals 0 as well based on Equation (11), which implies that the moiré pattern and graphene are translated in the same direction. For more general cases, if the graphene layer is rotated with a non-zero angle θ, there is an offset $-\theta + \varphi$ between α andγ.